



HAL
open science

Crustal Anisotropy in the Martian Lowlands From Surface Waves

C. Beghein, J. Li, E. Weidner, R. Maguire, J. Wookey, V. Lekić, Philippe
Lognonné, W. Banerdt

► **To cite this version:**

C. Beghein, J. Li, E. Weidner, R. Maguire, J. Wookey, et al.. Crustal Anisotropy in the Martian Lowlands From Surface Waves. *Geophysical Research Letters*, 2022, 49 (24), 10.1029/2022GL101508 . hal-03918294

HAL Id: hal-03918294

<https://u-paris.hal.science/hal-03918294>

Submitted on 2 Jan 2023

HAL is a multi-disciplinary open access archive for the deposit and dissemination of scientific research documents, whether they are published or not. The documents may come from teaching and research institutions in France or abroad, or from public or private research centers.

L'archive ouverte pluridisciplinaire **HAL**, est destinée au dépôt et à la diffusion de documents scientifiques de niveau recherche, publiés ou non, émanant des établissements d'enseignement et de recherche français ou étrangers, des laboratoires publics ou privés.

f

Crustal Anisotropy in the Martian Lowlands from Surface Waves

C. Beghein^{1*}, J. Li¹, E. Weidner¹, R. Maguire², J. Wookey³, V. Lekić⁴, P.
Lognonné⁵, W. Banerdt⁶

¹Department of Earth, Planetary, and Space Sciences, University of California Los Angeles, Los Angeles,
CA 90095

²Department of Geology, University of Illinois Urbana-Champaign, Urbana, IL 61801

³School of Earth Sciences, University of Bristol, Bristol, UK.

⁴Department of Geology, University of Maryland, College Park, MD 20742

⁵Université Paris Cité, Institut de physique du globe de Paris, CNRS, Paris, France

⁶Jet Propulsion Laboratory, California Institute of Technology, Pasadena, CA 91109, USA

Key Points:

- Rayleigh and Love waves were detected on Mars;
- Seismic wave speed is directionally dependent over large-scales within Mars crust;
- The shear wave horizontal velocity is faster than the vertical velocity at 10 – 25 km depth in the lowlands between the event and the lander.

*Department of Earth, Planetary, and Space Sciences, University of California Los Angeles

Corresponding author: C. Beghein, cbeghein@epss.ucla.edu

Abstract

The largest seismic event ever recorded on Mars, with a moment magnitude of 4.7 ± 0.2 , is the first event to produce both Love and Rayleigh wave signals. We measured their group velocity dispersion between about 15 s and 40 s period and found that no isotropic depth-dependent velocity model could explain the two types of waves simultaneously, likely indicating the presence of seismic anisotropy. Inversions of Love and Rayleigh waves yielded velocity models with horizontally polarized shear waves traveling faster than vertically polarized shear waves in the top 10 km – 25 km. We discuss the possible origins of this signal, including the preferred orientation of anisotropic crystals due to shear deformation, alignment of cracks, layered intrusions due to an impact, horizontal layering due to the presence of a large-scale sediment layer on top of the crust, and alternation of sedimentation and basalt layers deposits due to large volcanic eruptions.

Plain Language Summary

The largest marsquake recorded so far sent energy across the red planet in the form of different kinds of waves, including two types of waves trapped near the surface. This was the first time both types of so-called surface waves were detected on Mars. Combining measurements from these two types of surface waves allowed us to determine the speed of other types of waves, i.e. waves that travel horizontally and that make rocks move perpendicular to the direction of propagation. We found that these waves move faster in the crust between 10 km and 25 km depth when the rocks oscillate in a direction sub-parallel to the planet surface than if the rocks vibrate in the vertical direction. This wave speed dependence can tell us about deformation mechanisms inside the crust. We found that either an alternation of volcanic rocks and sediments layers due to volcanic eruptions or internal layering within the crust due to an impact are the preferred explanations for our observations.

1 Introduction

The largest seismic event ever detected on Mars occurred on May 4 2022, and was recorded by the Seismic Experiment for Interior Structure (SEIS) Very Broadband (VBB) seismometer (Lognonné et al., 2020) of NASA’s InSight mission (Banerdt et al., 2020). The event, labeled S1222a, occurred at 23:23:06.57 UTC (sol 1222) and has a moment

47 magnitude M_w estimated at 4.7 ± 0.2 (Kawamura et al., 2022). This event is thus five
 48 times larger than the second largest event recorded (Horleston et al., 2022) and had enough
 49 energy to allow for the first direct observation of multi-orbiting Rayleigh waves on Mars
 50 (Panning et al., 2022). Based on their calculated back azimuth of 101° (with a range of
 51 $96^\circ - 112^\circ$) and epicentral distance ($37^\circ \pm 1.6^\circ$), the Mars Quake Service (MQS) deter-
 52 mined that this quality A (InSight Marsquake Service, 2020) event originated at 7.63° S,
 53 170.67° E, near the North-South dichotomy, east of the landing site, and south of Cer-
 54 berus Fossae (Fig. 1).

55 Most remarkably, S1222a generated surface waves clearly observable on all three
 56 components of the ground motion (Fig. 2). While Rayleigh waves have been previously
 57 detected on Mars with impact events S1000a and S1094b (Kim et al., 2022), no Love waves
 58 had been seen before. Since Rayleigh and Love waves are predominantly sensitive to dif-
 59 ferent elastic parameters (governing the speed of vertically and horizontally polarized
 60 shear waves travelling horizontally, respectively), this gives us an opportunity to study
 61 the presence of large-scale radial seismic anisotropy on Mars between the lander and the
 62 event epicenter. Radial anisotropy, which is a type of transverse isotropy with a verti-
 63 cal symmetry axis, manifests as a difference in the velocities of vertically (V_{SV}) and hor-
 64 izontally (V_{SH}) polarized shear waves. It is quantified by parameter $\xi = V_{SH}^2/V_{SV}^2$ and
 65 is a powerful tool to study the deformation history of a planet (e.g. Weiss et al. (1999)).

66 **2 Data Analysis**

67 We first removed the instrument response from the raw data to get the velocity record,
 68 and rotated the U, V, and W components of the SEIS instrument to N, E, and Z. We
 69 then rotated the N and E components to the radial (R) and tangential (T) coordinates
 70 using a back azimuth of 101° as determined by the MQS (Kawamura et al., 2022). The
 71 waveforms display clear wave packets on the Z and R components, characteristic of Rayleigh
 72 waves, and a wave packet on the T component, identified as a Love wave (Fig. 2(a)). Us-
 73 ing two-pass, second-order Butterworth filters in different frequency bands (10 – 20 s,
 74 15 – 25 s, 20 – 30 s, 25 – 30 s, and 30 – 40 s), we found that S1222a generated surface
 75 wave energy at periods between about 10 s and 40 s on all components of the seismo-
 76 gram (Fig. S1).

77 We subsequently carried out a multiple filter analysis (MFT) of the Z, R, and T
 78 components to isolate the group velocities as a function of time (Dziewonski et al., 1969;
 79 Herrmann, 2013). This consists in narrow bandpass filters using the operator $\exp[-\alpha(\omega - \omega_0)^2/\omega_0^2]$
 80 where ω_0 is the center frequency. Parameter α compromises between resolution in the
 81 time and frequency domains. We measured the group velocities by picking the maximum
 82 energy of the waveform envelope for each period (Fig. 2(b) – (d)). The velocity uncer-
 83 tainty is defined by a threshold energy of at least 1 dB of the energy maxima as in Beghein
 84 et al. (2010). The MFT analysis shows that Rayleigh waves have peak energy between
 85 about 15 s and 40 s period and group velocities increasing continuously up to about ~ 3 km/s
 86 (Fig. 2(b) – (c)). The transverse component displays peak Love wave energy in the same
 87 period range but with faster group velocities between about 3.2 km/s and 3.5 km/s (Fig. 2(d)).
 88 We note that the T component MFT plot differs from the Z and R components in that
 89 its dispersion curve first decreases between 10 s and 15 s and becomes relatively flat at
 90 greater periods.

91 We tested that the effect of back azimuth uncertainties on the dispersion curves
 92 and found no significant change (Fig. S2). We also performed an ellipticity analysis in
 93 different period bands (Fig. S3). The elliptical and retrograde motion found between 15 s
 94 and 35 s confirm the Rayleigh wave nature of the signal.

95 We additionally observe discrepancies in the Rayleigh wave group velocities between
 96 the Z and R components at periods >30 s, and even more so at periods >35 s for which
 97 there is little overlap between the error bars (Fig. 2 and Fig. S3(a)). These differences
 98 could be due to the lower waveform amplitude along the R component (Fig. S3(b)), mak-
 99 ing it more easily contaminated by noise. We considered stacking the R and Hilbert-transformed
 100 Z components to improve the signal-to-noise ratio and obtain more reliable and consis-
 101 tent group velocities at periods >30 s. However, our ellipticity analysis showed that, while
 102 at short period (15 – 30 s) the phase shift between the Z and R components is about 90°
 103 (i.e., the major and minor axes of the ellipse are not parallel to the x- or y-axis), it is
 104 not the case at 30 – 35 s, indicating that applying a Hilbert transform will not help. At
 105 periods of 35 – 40 s, although the phase shift is close to 90° , the ellipticity (i.e., the ra-
 106 tio between Z and R) is much larger than that at short periods due to smaller ampli-
 107 tudes on the R component and may we not have a reliable signal. Because of these dis-
 108 crepancies between the Z and R components, we chose to invert measurements up to 30 s

109 only. Inversions including all periods were performed for comparison. They are presented
 110 in the Supplementary Material and discussed in section 4.

111 The presence of transient signals, including glitches due to diurnal temperature vari-
 112 ations on Mars, has the potential to contaminate the waveforms (e.g. Kim, Davis, et al.
 113 (2021)). We performed a glitch detection on the raw data using a synthetic glitch tem-
 114 plate (Scholz et al., 2020) and found no glitches near the first minor-arc surface wave ar-
 115 rivals (Fig. S4).

116 **3 Method**

117 The measured Love and Rayleigh wave dispersion curves were inverted jointly to
 118 obtain one-dimensional (1-D) V_{SV} and V_{SH} models representing the average structure
 119 between the station and the quake. The V_{SH} and V_{SV} model distributions were then com-
 120 bined to calculate radial anisotropy ξ . We used the Computer Programs in Seismology
 121 (Herrmann, 2013) code package to generate the synthetic group velocity, and a Niche
 122 Genetic Algorithm for the inversion (Koper et al., 1999; Li et al., 2021) together with
 123 a B-spline parameterization, as described below. The results obtained with this approach,
 124 hereafter referred to as Method 1, were compared against results from two other tech-
 125 niques (Method 2 and Method 3). Method 2 is a fully non-linear transdimensional hi-
 126 erarchical Bayesian approach using a reversible jump Monte Carlo Markov Chain (MCMC)
 127 algorithm and a layered parameterization that is allowed to vary at each iteration (Weidner
 128 et al., 2022). Method 3 also uses a MCMC approach but the parameterization is fixed
 129 and uses B-splines. These methods are described in more details in the Supplementary
 130 Material.

131 The period range at which the detected surface waves display strong energy (15
 132 – 30 s) corresponds to sensitivity to structure in the upper $\sim 70 - 80$ km, though it is im-
 133 portant to note that Love wave sensitivity to V_{SH} is greatly reduced below 50 km (Fig. S5).
 134 Anisotropy was thus allowed in the models down to 80 km depth.

135 In the 0 – 80 km depth range, the V_{SV} and V_{SH} profiles were characterized by eight
 136 third-order B-splines. Since Rayleigh waves display some sensitivity down to about 130 km,
 137 we also inverted for isotropic shear wave velocities between 80 km and 130 km with a depth
 138 interval of 20 km for the depth anchor points. The prior constraint for all the shear wave
 139 velocities were uniform distributions from 1.5 km/s to 4.5 km/s. At depths greater than

140 130 km, we used the InSight model KKS21GP, which was extracted from the models of
 141 Khan et al. (2021) and Stähler et al. (2021) and selected to have a crust comparable to
 142 that of Knapmeyer-Endrun et al. (2021). The V_P/V_S ratio was set to be 1.80 and the
 143 density-to- V_S ratio was assumed to be 0.8. This choice was based on the ratios of the
 144 receiver function study of Knapmeyer-Endrun et al. (2021), which are between 1.7 to 1.9
 145 for V_P/V_S and 0.7 to 0.9 for density-to- V_S . In total, we searched for 200,000 models dur-
 146 ing the inversion, and the acceptable models were selected if their predicted group ve-
 147 locity at each period fits the measurements within uncertainties. The posterior distri-
 148 butions are based on these best data fitting models.

149 4 Results

150 We first inverted the Rayleigh wave dispersion curve and used the resulting 1-D
 151 models to predict Love wave dispersion, and vice versa (Fig. S6). It is clear that isotropic
 152 models obtained with the Rayleigh wave data are unable to explain the measured Love
 153 wave dispersion and that the models obtained from Love waves alone cannot represent
 154 the Rayleigh wave measurements. This same behavior has been widely observed in Earth's
 155 upper mantle: Love waves usually have larger phase velocities than predicted by isotropic
 156 models that fit Rayleigh wave phase velocities. It has also been detected in the conti-
 157 nental crust (e.g., Moschetti et al. (2010)). This apparent Love-Rayleigh discrepancy was
 158 first observed on Earth by Anderson (1961) and can be resolved by introducing trans-
 159 verse isotropy in the model (Harkrider & Anderson, 1962). We thus performed joint Love
 160 and Rayleigh wave inversions for V_{SH} and V_{SV} as described in section 3, and calculated
 161 the resulting anisotropy ξ and Voigt V_S average model distributions: $V_S = \sqrt{(2V_{SV}^2 + V_{SH}^2)/3}$
 162 (Babuska & Cara, 2012).

163 Our average velocity models in the top 5 km and below 30 km depth exhibit sig-
 164 nificant uncertainties and variability between the different methods. The velocity obtained
 165 with Method 1 at shallow depths is around 3.0 ± 0.1 km/s. V_S then increases to 3.2 ± 0.06 km/s
 166 around 20 km depth and reaches 3.4 ± 0.1 km/s around 40 km below the surface. For
 167 Method 2, the V_S models are characterized by about two layers with $V_S = 3.2 \pm 0.1$ km/s
 168 in the top 20 – 30 km and $V_S = 3.4 \pm 0.2$ km/s below, down to 50 km depth. With
 169 Method 3, V_S increases from 2.5 ± 0.3 km/s to 3.0 ± 0.75 km/s within the top 5 km,
 170 $V_S = 3.4 \pm 0.8$ km/s at 20 km depth and $V_S = 3.5 \pm 0.2$ km/s at 40 km.

171 Our results also show a clear $V_{SH} > V_{SV}$ signal with $\xi \simeq 1.1$ between 5 km and
 172 ~ 30 km depth (Fig. 3), consistent across all three methods within uncertainties (Figs. S7
 173 and S8). The posterior model uncertainties do not, however, rule out $V_{SH} < V_{SV}$ in
 174 the top 5 km and deeper than about 30 km. We additionally performed synthetic tests
 175 that confirmed these results: In Fig. S9, we created and inverted an input model with
 176 Method 1 that contained 10 % anisotropy in the 0 – 10 km depth range, 20 % at 10 – 30 km
 177 depth, and 10 % at 30 – 50 km. The model was isotropic at greater depths. The output
 178 revealed that, while the positive anisotropy is well recovered in the 10 – 25 km depth range,
 179 several solutions of opposite sign were found at shallower and greater depths. The lack
 180 of resolution in the top 5 – 10 km is likely due to the sensitivity of the data at the pe-
 181 riod range for which we have measurements. Shorter period data would be able to bet-
 182 ter constrain the shallower depths but have not been reliably recorded with the event
 183 analyzed here.

184 Fig. 3 corresponds to inversions including only the Rayleigh wave data that were
 185 consistent between the Z and R components, i.e. up to 30 s period. For completeness,
 186 we also inverted the data measured on the Z and R separately up to 40 s (Fig. S10). These
 187 tests show that including periods above 30 s yields model uncertainties that depend on
 188 which component the Rayleigh waves are measured. In addition, while most models still
 189 display $\xi > 1$ between 10 km and 25 km, the error bars are significantly larger. This
 190 dependence of the models on the data at periods greater than 30 s validates our deci-
 191 sion to only present results based on the shorter period data in Fig. 3.

192 5 Discussion

193 5.1 Seismic Velocities

194 Lognonné et al. (2020) discussed the rock types, including sedimentary, impact-related,
 195 and volcanic, and their associated seismic velocities in the Martian crust around the In-
 196 Sight landing site. They found that the low velocities they had obtained for the shal-
 197 lowest crustal layer (upper ~ 8 km) suggest altered and/or damaged upper volcanic rocks.
 198 The velocities in the underlying layer (around 8 – 20 km depth), with $V_P = 4.5 - 6$ km/s
 199 and $V_S = 2.5 - 3.3$ km/s, were consistent with altered, iron-rich basaltic rocks. Simi-
 200 lar velocities were later found by Knapmeyer-Endrun et al. (2021).

201 In our study, Methods 1 and 2 predict $V_S = 3.0 \pm 0.1$ km/s and $V_S = 3.2 \pm 0.1$ km/s,
 202 respectively, in the top 5 – 10 km, which is larger than the 1.7 – 2.1 km/s estimated by
 203 Lognonné et al. (2020) and Knapmeyer-Endrun et al. (2021) at the landing site. Method
 204 3 gives lower V_S values between 2.5 ± 0.3 km/s and 3.0 ± 0.75 km/s in that depth
 205 range, but they are still larger than found beneath the lander. Using $V_P/V_S = 1.8$ (Knapmeyer-
 206 Endrun et al., 2021), we calculated that this corresponds to $V_P = 4.5 - 5.4$ km/s, which
 207 is still compatible with damaged or altered basalt, but also with impact melt, impact
 208 breccia, and sandstone (Lognonné et al., 2020).

209 Between ~ 10 km and 30 km depth, V_S is consistent among the three methods with
 210 values around 3.1 – 3.5 km/s. Using a $V_P/V_S = 1.8$ (Knapmeyer-Endrun et al., 2021),
 211 this correspond to $V_P \simeq 5.6 - 6.3$ km/s. Compared to Lognonné et al. (2020), our ve-
 212 locity models at those depths are thus compatible with volcanic rocks (damaged, altered,
 213 or compact basalt) and with impact melt.

214 5.2 Seismic Anisotropy

215 The presence of seismic anisotropy, i.e. the directional dependence of seismic wave
 216 velocity, is well documented on Earth (Dziewonski & Anderson, 1981; Montagner, 1994).
 217 In Earth’s upper mantle, it is considered a strong indicator of past (in the mantle litho-
 218 sphere) or present (in the asthenosphere) strain coherent over large scales, resulting in
 219 textural changes such as lattice or crystal preferred orientation (LPO or CPO) of intrin-
 220 sically anisotropic olivine crystals due to mantle deformation (Nishimura & Forsyth, 1989;
 221 Karato & Wu, 1993; Montagner, 1998; Becker et al., 2003; Yuan & Romanowicz, 2010).

222 In Earth’s crust, seismic anisotropy is often attributed to the shape preferred ori-
 223 entation (SPO) of isotropic material with contrasting elastic properties (Backus, 1962),
 224 such as the preferred alignment of melt pockets or lenses (Bastow et al., 2010), the dis-
 225 tribution of fluid-filled cracks, or preferentially oriented pore spaces (Crampin, 1981; Crampin
 226 & Booth, 1985; Crampin, 1989). SPO can be caused by sedimentary layering, magmatic
 227 intrusions, or the presence of faults. In this case, the observed large-scale seismic anisotropy
 228 represents the effective medium comprised of unmapped fine (subwavelength thickness)
 229 isotropic layered structures (Backus, 1962). Alternatively, observations of anisotropy with
 230 $V_{SH} > V_{SV}$ in Earth’s mid-to-lower continental crust are often attributed to the align-
 231 ment of minerals such as mica in ductile flow (e.g., Brownlee et al. (2017)). In Tibet, for

232 instance, it has been proposed that this type of anisotropy could be due to underthrust-
 233 ing of the Indian crust beneath Tibet or could result from ongoing crustal thinning (Shapiro
 234 et al., 2004).

235 Our results indicate a robust seismic anisotropy signal in the 10 – 30 km depth range
 236 (Fig. 3). Constraints from gravity data show that the crustal thickness along the event-
 237 station path, which samples the lowlands, is around 40 km (Wieczorek et al., 2022). In
 238 addition, recent P- and S-wave receiver function analyses with seismic data collected by
 239 SEIS have shown that the crustal thickness at the lander site is between 20 km and 40 km
 240 (Knapmeyer-Endrun et al., 2021), with a preference for 40 km with PP receiver func-
 241 tions (Kim, Lekić, et al., 2021).

242 In order to observe seismic anisotropy, there needs to be coherent preferred orien-
 243 tation over large distances. Specifically, producing $V_{SH} > V_{SV}$ would require either the
 244 preferential horizontal alignment of fast axes of anisotropic minerals or cracks. There-
 245 fore, we rule out the alignment of cracks (Crampin, 1981; Crampin & Booth, 1985; Crampin,
 246 1989) as a likely explanation for the observed signal since alignment of vertically-oriented
 247 cracks would yield $V_{SV} > V_{SH}$. In addition, at depths greater than about 20 km, the
 248 pressure is such that cracks tend to close.

249 Another possibility is horizontal layering of isotropic material (with layer thicknesses
 250 much smaller than the dominant wavelength), i.e. extrinsic or apparent anisotropy. Where
 251 the different layers have contrasting elastic properties, an overall anisotropic medium re-
 252 sults. In order to assess the degree of heterogeneity required, we have performed some
 253 simple calculations using Backus averaging (Backus, 1962). Fig. S11 shows the result-
 254 ing ξ parameter for a range of degrees of shear wave velocity perturbations, and layer
 255 thickness ratios. Producing an anisotropic signal compatible with our observations re-
 256 quires a relative velocity perturbation of $\sim 20\%$, when fast and slow layer thicknesses
 257 are approximately equal. As either material begins to dominate the ensemble, the re-
 258 quired perturbation significantly increases. Such a mechanism is observed in sedimen-
 259 tary basins on Earth (Sayers, 1998). On Mars, there is evidence for past floods and sed-
 260 imentary transportation near the rim at the Pathfinder landing site (Rodriguez et al.,
 261 2019), as well as the presence of rivers and even an ocean that may have had enough wa-
 262 ter to fill the Vastitas Borealis, the Northern basin in the upper hemisphere (Carr & Head III,
 263 2003; Di Achille & Hynek, 2010; Villanueva et al., 2015). Such a standing body of wa-

264 ter could have deposited sediments over large distances (Head et al., 2001). However,
265 McLennan (2012) estimated the global average thickness of the sediment layer to be less
266 than 2 km. Although the sedimentary rocks at several locations can reach greater depths,
267 they are shallower than 10 km in many places (e.g., 5 km in Gale crater (Grotzinger et
268 al., 2015), 3 – 6 km in Juventae Chasma (Grotzinger & Milliken, 2012), and 3 km in Med-
269 uase Fossae (Bradley et al., 2002). Therefore, the observed anisotropy at depth between
270 10 km and 30 km is unlikely due to sedimentary rocks alone unless they extend to much
271 greater depths than expected.

272 Layered sill complexes have been suggested to produce strong ($> 8\%$) positive ra-
273 dial anisotropy at 5 – 18 km depth below silic calderas (Jiang et al., 2018), but it is usu-
274 ally very localized in depth and spatial extent. The strength and extent of the anisotropy
275 observed here would require a lot of melt distributed in the Martian crust over a broad
276 depth range. Alternatively, with Mars hosting the largest volcano of the solar system north-
277 east of InSight, Olympus Mons, as well as Elysium Mons to the north, multiple volcanic
278 events over broad scales could have led to an alternation of basalt layers deposit and sed-
279 imentation, which could potentially have generated radial anisotropy, though, again, it
280 would have to extend over rather large depths. Basalt packages in a terrestrial context
281 (for example, those associated with large igneous provinces, e.g., Planke (1994); Christie
282 et al. (2006)) show a high degree of velocity layering, variation within which easily ex-
283 ceeds the 20 % perturbation required to reproduce our inferred ξ value (Baan et al., 2007).
284 Much of this heterogeneity is associated with variations of porosity and sub-aerial frac-
285 turing (Planke, 1994) which might be expected to be reduced at greater depth in the Earth.
286 It has been suggested, however, that on Mars pore space might persist to the observed
287 seismic discontinuity at 20 km below the InSight lander (Knapmeyer-Endrun et al., 2021;
288 Wieczorek et al., 2022).

289 Another option is the presence of layered intrusions due to a single or multiple im-
290 pacts (Wilhelms & Squyres, 1984; Nimmo & Tanaka, 2005; Andrews-Hanna et al., 2008;
291 Marinova et al., 2008). It has been proposed that the crustal dichotomy, characterized
292 by a difference of up to 30 km in crustal thickness between the northern lowlands and
293 the southern highlands, corresponds to a crater formed by a large impact. Such an im-
294 pact could have contributed to the evolution of the proto-crust on Mars and other ter-
295 restrial planets, and could have caused internal layering within the crust. This has been
296 shown to be the case on Earth: Latypov et al. (2019) studied the exposed impact melt

297 sheet of the Sudbury Igneous Complex located in Canada and showed that such ancient
298 and compositionally primitive Hadean impact melt sheets underwent large-scale igneous
299 differentiation.

300 This scenario is also consistent with the results of Li, Beghein, Lognonné, et al. (2022)
301 who constrained crustal V_{SV} in the highlands by measuring and inverting the dispersion
302 of minor-arc (R1) and major-arc (R2) Rayleigh waves, i.e. the wave that travels the short-
303 est and the longest distance, respectively, along the great circle path between the epi-
304 center and the instrument, according to ray theory. They found V_{SV} between about 3.3 km/s
305 and 3.5 km/s in the highlands, which is greater than the crustal V_{SV} of 3.0 – 3.2 km/s
306 found here in the lowlands, but similar to the 3.4 km/s we found for crustal V_{SH} in the
307 lowlands (Fig. S8(b), S8(e), and S8(h)). This similarity in velocity between V_{SH} in the
308 lowlands and V_{SV} in the highlands could indicate that the average Martian upper crustal
309 shear wave velocities might have been originally similar in the lowlands and highlands.
310 The impact-related horizontal melt sheets created at depth in the lowlands could have
311 lowered the shear wave velocity in the vertical direction (i.e., V_{SV}) but left V_{SH} unchanged
312 (Fig. S12(a)).

313 Finally, we cannot entirely rule out the lattice preferred orientation of anisotropic
314 crystals in the Martian crust to explain the observed signal, as proposed for Earth’s mid-
315 to-lower continental crust (Shapiro et al., 2004). There is currently no large underthrust-
316 ing on Mars such as that seen in Tibet (Shapiro et al., 2004), and there is no evidence
317 of large-scale crustal thinning between the lander and the event epicenter, but one could
318 envision that anisotropic crystal fabrics could be preserved in the crust from past defor-
319 mation such as an impact. If the impact melted the crust and it began to flow, fabric
320 could have been generated over relatively large-scales and become frozen-in as rocks cooled
321 down.

322 We end this discussion by pointing out that, importantly, the observed anisotropy
323 ($\xi > 1$) in this study does not contradict the previously observed anisotropy beneath
324 the InSight lander site (Li, Beghein, Wookey, et al., 2022). First, the anisotropy in Li,
325 Beghein, Wookey, et al. (2022) reflects the local structure (i.e., within 30 km) beneath
326 the lander, and this study represents the average structure along the $> 2,000$ km long
327 path between the epicenter and the station. Second, the anisotropy in Li, Beghein, Wookey,
328 et al. (2022) was restricted to the topmost layer (around 8 km), whereas the most re-

329 liably resolvable depths in the present study are 10 – 25 km. Last, but importantly, the
 330 direction of the ray path is near-vertical for the body waves in Li, Beghein, Wookey, et
 331 al. (2022) and is horizontal for the surface waves in this study. Therefore, the shear-wave
 332 velocity we constrain from the surface waves is that of a horizontally propagating shear-
 333 wave. The definitions of V_{SV} are not thus the same in both studies since the directions
 334 of the polarization of the SV waves (perpendicular to the direction of the seismic rays)
 335 are different (Fig. S12(b) – (c)). Subsequently, the $V_{SV} < V_{SH}$ anisotropy in this study
 336 does not contradict the $V_{SV} > V_{SH}$ anisotropy in Li, Beghein, Wookey, et al. (2022)
 337 and they reflect different properties of the materials in the Martian crust. In fact, the
 338 modeling done by Li, Beghein, Wookey, et al. (2022) to explain their observations used
 339 a horizontally transverse isotropic medium, which reflects the presence of azimuthal anisotropy.
 340 Here, the signal reflects radial anisotropy, also called polarization anisotropy or verti-
 341 cally transverse isotropy (VTI), which has hexagonal symmetry with a vertical symme-
 342 try axis. The observations beneath the lander require a medium with a higher degree
 343 of symmetry.

344 6 Conclusion

345 We analyzed the Rayleigh and Love waves generated by the largest event ever recorded
 346 on Mars. The waveforms contain surface wave energy on all three components of the seis-
 347 mogram at periods between 15 s and 40 s. We measured the group velocity dispersion
 348 of these waves on the vertical, radial, and transverse components of the seismogram us-
 349 ing a multiple filter analysis. We found that Rayleigh waves group velocities increase con-
 350 tinuously up to about 3 km/s between 15 s and 40 s period. Love wave group velocities
 351 are systematically larger, between about 3.2 km/s and 3.5 km/s in the 15 – 40 s period
 352 range. Because of a discrepancy between the Rayleigh wave group velocities in the trans-
 353 verse and vertical directions at periods greater than 30 s, we only used data up to 30 s.

354 Isotropic inversions of the Love wave data were unable to explain the Rayleigh wave
 355 data and vice versa. The Love and Rayleigh wave dispersion curves were thus inverted
 356 jointly for shear wave velocities and radial anisotropy. We found a well-resolved signal
 357 in the crust, with $V_{SH} > V_{SV}$ ($\xi > 1$) between 10 km and 25 km depth.

358 LPO of anisotropic crystals inside the crust is difficult to reconcile with our cur-
 359 rent knowledge of the martian crust as it would require a large-scale shear mechanism

360 such as crustal thinning or underthrusting. However, we could be seeing frozen-in fab-
361 ric due to melting followed by flow (and thus LPO) in the crust after an impact, for in-
362 stance. The observed anisotropy may alternatively be apparent rather than intrinsic. We
363 rule out cracks as a possible explanation for this signal since vertical cracks would yield
364 $V_{SH} < V_{SV}$. Horizontal layering of sediments is unlikely to explain the signal as well
365 because they would not extend to great enough depths. Our preferred explanations in-
366 clude an alternation of isotropic basalt layers deposit and sedimentation caused by vol-
367 canic eruptions, or the presence of isotropic layered intrusions due to an impact.

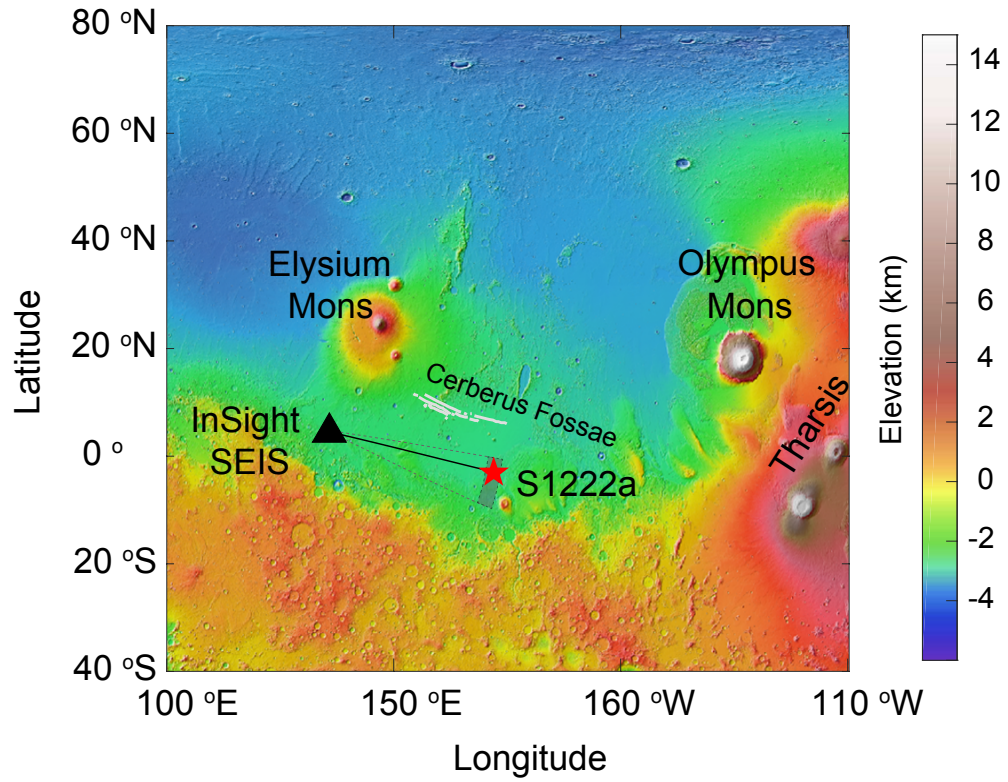


Figure 1. Location of event S1222a (red star) and SEIS (black triangle). The grey shaded area represents the uncertainties in back azimuth and epicentral distance and the three black curves are possible great circle paths of the surface waves.

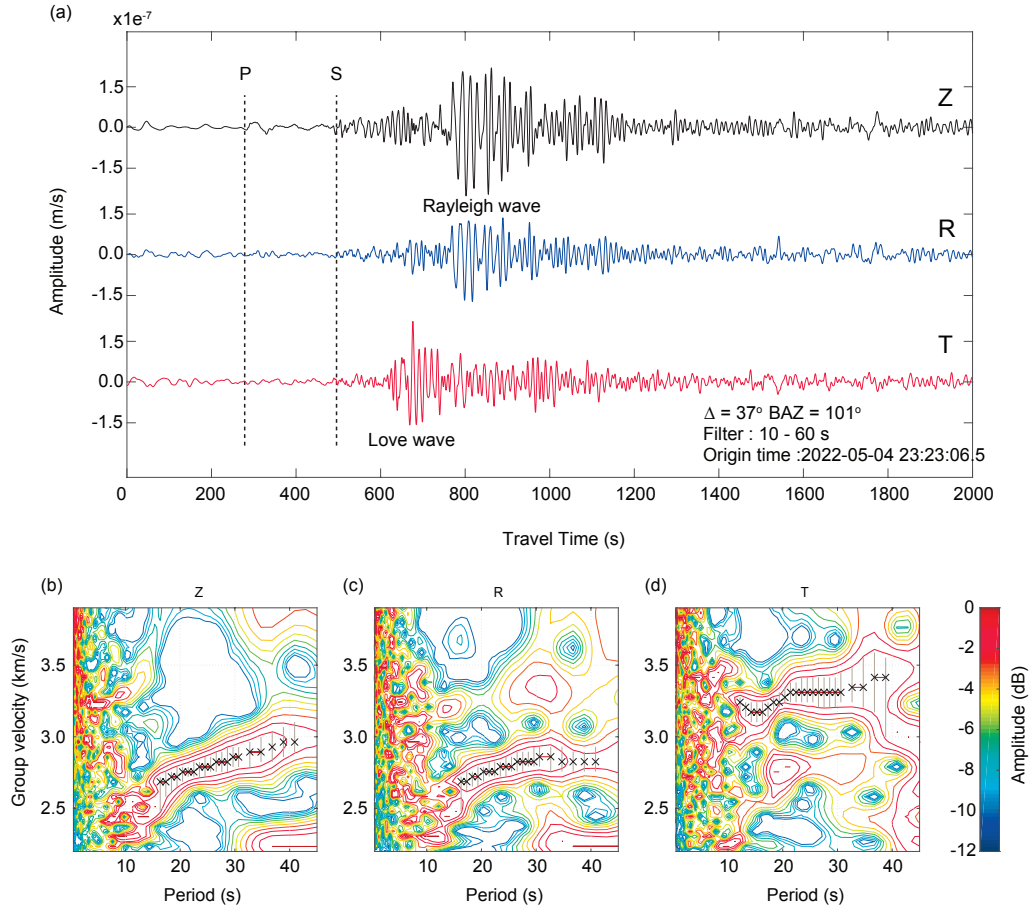


Figure 2. (a) Deglitched waveforms on the to Z, R, T coordinates. A second order, zero-phase shift bandpass filter was applied between 10 s and 60 s period. (b)-(d) Multiple filter analysis of the vertical (a), radial (b), and tangential (c) components of the VBB.

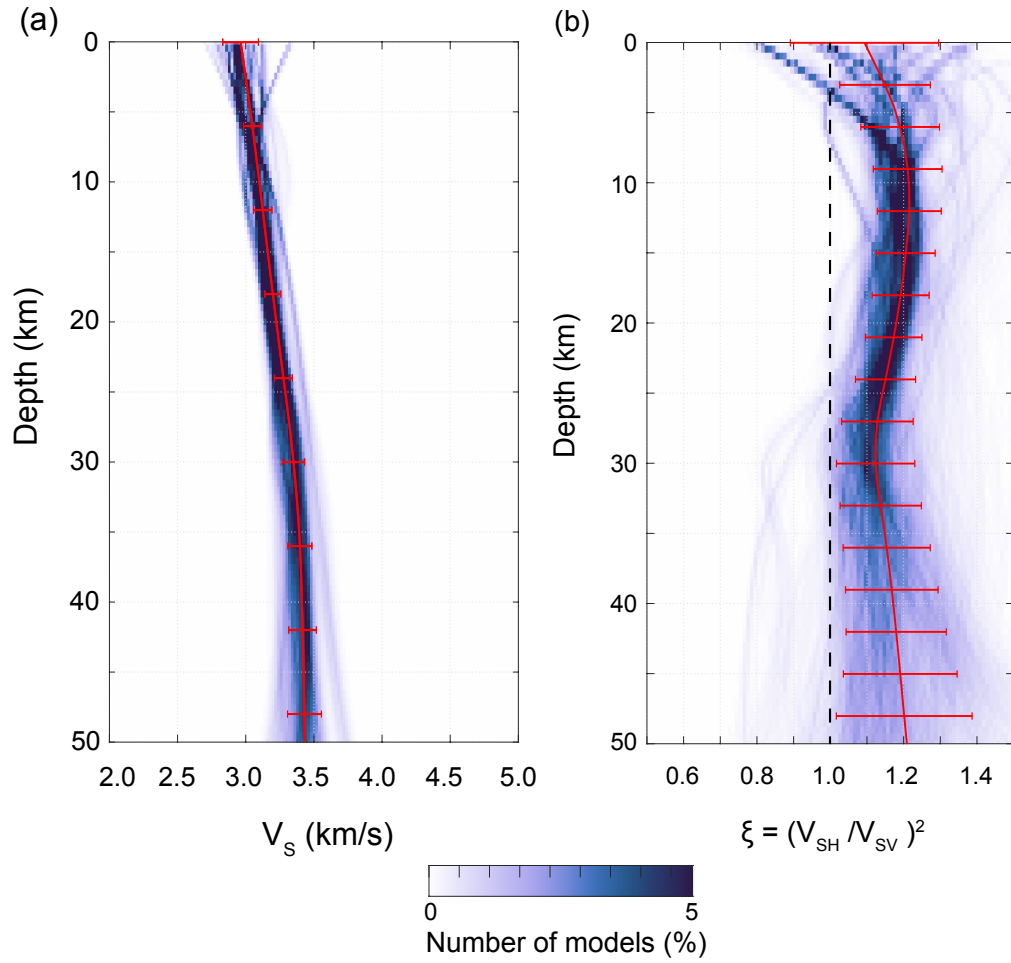


Figure 3. V_S (a) and ξ (a) models resulting from Method 1 applied to the measured dispersion curves. The vertical black dashed line in (b) represents an isotropic model for reference. The red horizontal bars are the uncertainties calculated by averaging the variance obtained by each of the three methods.

7 Open Research

Data and materials availability: The InSight event catalogue (Clinton et al., 2021; Ceylan et al., 2022; InSight Marsquake Service, 2022a, 2022b) and waveform data are available from the IRIS-DMC, NASA-PDS (InSight Mars SEIS Data Service, 2019a) and IGP data center (InSight Mars SEIS Data Service, 2019b).

Acknowledgments

We thank Dr. Caroline Eakin and Dr. Joshua Russell for their constructive reviews of our manuscript. C.B. also wishes to thank Dr. Jeremy W. Boyce for the discussions that helped with the interpretation of our results.

We acknowledge NASA, CNES, their partner agencies and Institutions (UKSA, SSO, DLR, JPL, IGP-CNRS, ETHZ, IC, MPS-MPG) and the flight operations team at JPL, SISMOC, MSDS, IRIS-DMC and PDS for providing SEED SEIS data. This is ICN 271.

This research was carried out in part at the Jet Propulsion Laboratory, California Institute of Technology, under a contract with the National Aeronautics and Space Administration (80NM0018D0004). C. B., J. L., and E. W. were funded by NASA InSight PSP grant #80NSSC18K1679. J.W. was funded by UKSA Aurora grant ST/T002972/1. PL is funded by the french space agency, CNES and by Agence Nationale de la recherche (ANR-19-CE31-0008-08 and ANR-18-IDEX-0001).

The authors declare that they have no competing interests.

References

- Anderson, D. L. (1961). Elastic wave propagation in layered anisotropic media. *J. Geophys. Res.*, *66*(9), 2953 – 2963. doi: 10.1029/jz066i009p02953
- Andrews-Hanna, J. C., Zuber, M. T., & Banerdt, W. B. (2008). The borealis basin and the origin of the martian crustal dichotomy. *Nature*, *453*(7199), 1212–1215.
- Baan, M. v. d., Wookey, J., & Smit, D. (2007). Stratigraphic filtering and source penetration depth. *Geophysical Prospecting*, *55*(5), 679 – 684.
- Babuska, V., & Cara, M. (2012). *Seismic Anisotropy in the Earth*. Springer Netherlands. Retrieved from <https://books.google.com/books?id=qhnRBgAAQBAJ>
- Backus, G. E. (1962). Long-wave elastic anisotropy produced by horizontal layering. *J. Geophys. Res.*, *67*(11), 4427–4440. doi: 10.1029/JZ067i011p04427

- 399 Banerdt, W. B., Smrekar, S. E., Banfield, D., Giardini, D., Golombek, M., Johnson,
400 C. L., ... Wicczorek, M. (2020). Initial results from the InSight mission on
401 Mars. *Nat. Geosci.*, *13*, 183–189. doi: 10.1038/s41561-020-0544-y
- 402 Bastow, I. D., Pilidou, S., Kendall, J.-M., & Stuart, G. W. (2010). Melt-
403 induced seismic anisotropy and magma assisted rifting in ethiopia: Evidence
404 from surface waves. *Geochemistry, Geophysics, Geosystems*, *11*(6). doi:
405 10.1029/2010GC003036
- 406 Becker, T. W., Kellogg, J. B., Ekström, G., & O'Connell, R. J. (2003). Compari-
407 son of azimuthal seismic anisotropy from surface waves and finite strain from
408 global mantle circulation models. *Geophysical Journal International*, *155*(2),
409 696 – 714. doi: 10.1046/j.1365-246x.2003.02085.x
- 410 Beghein, C., Snoke, J. A., & Fouch, M. J. (2010). Depth constraints on azimuthal
411 anisotropy in the Great Basin from Rayleigh-wave phase velocity maps. *Earth
412 and Planetary Science Letters*, *289*(3-4), 467 – 478. doi: 10.1016/j.epsl.2009.11
413 .036
- 414 Bradley, B. A., Sakimoto, S. E. H., Frey, H., & Zimbelman, J. R. (2002).
415 Medusae Fossae Formation: New perspectives from Mars Global Sur-
416 veyor. *Journal of Geophysical Research: Planets*, *107*(E8), 2-1-2-17. doi:
417 10.1029/2001JE001537
- 418 Brownlee, S. J., Schulte-Pelkum, V., Raju, A., Mahan, K., Condit, C., & Orlandini,
419 O. F. (2017). Characteristics of deep crustal seismic anisotropy from a com-
420 pilation of rock elasticity tensors and their expression in receiver functions.
421 *Tectonics*, *36*(9), 1835-1857. doi: <https://doi.org/10.1002/2017TC004625>
- 422 Carr, M. H., & Head III, J. W. (2003). Oceans on mars: An assessment of the obser-
423 vational evidence and possible fate. *Journal of Geophysical Research: Planets*,
424 *108*(E5). doi: <https://doi.org/10.1029/2002JE001963>
- 425 Ceylan, S., Clinton, J. F., Giardini, D., Stähler, S. C., Horleston, A., Kawamura,
426 T., ... Banerdt, W. B. (2022). The marsquake catalogue from insight,
427 sols 0 – 1011. *Phys. Earth Planet. Inter.*, 106943. doi: [https://doi.org/10.1016/
428 j.pepi.2022.106943](https://doi.org/10.1016/j.pepi.2022.106943)
- 429 Christie, P., Gollifer, I., & Cowper, D. (2006). Borehole seismic studies of a volcanic
430 succession from the Lopra-1/1A borehole in the Faroe Islands, northern North
431 Atlantic. *Geological Survey of Denmark and Greenland (GEUS) Bulletin*, *9*,

- 432 23–40. doi: 10.34194/geusb.v9.4856
- 433 Clinton, J., Ceylan, S., van Driel, M., Giardini, D., Stähler, S. C., Böse, M.,
 434 ... Stott, A. E. (2021). The Marsquake catalogue from InSight, sols
 435 0–478. *Physics of the Earth and Planetary Interiors*, 310, 106595. doi:
 436 10.1016/j.pepi.2020.106595
- 437 Crampin, S. (1981). A review of wave motion in anisotropic and cracked
 438 elastic-media. *Wave Motion*, 3(4), 343–391. doi: [https://doi.org/10.1016/
 439 0165-2125\(81\)90026-3](https://doi.org/10.1016/0165-2125(81)90026-3)
- 440 Crampin, S. (1989). Suggestions for a consistent terminology for seismic anisotropy.
 441 *Geophysical Prospecting*, 37(7), 753–770. doi: [https://doi.org/10.1111/j.1365-
 442 -2478.1989.tb02232.x](https://doi.org/10.1111/j.1365-2478.1989.tb02232.x)
- 443 Crampin, S., & Booth, D. C. (1985). Shear-wave polarizations near the North Ana-
 444 tolian Fault, II. Interpretation in terms of crack-induced anisotropy. *Geophys.
 445 J. Int.*, 83(1), 75–92. doi: 10.1111/j.1365-246X.1985.tb05157.x
- 446 Di Achille, G., & Hynek, B. (2010). Ancient ocean on Mars supported by global dis-
 447 tribution of deltas and valleys. *Nature Geoscience*, 3, 459 – 463. doi: 10.1038/
 448 ngeo891
- 449 Dziewonski, A. M., & Anderson, D. L. (1981). Preliminary reference Earth model.
 450 *Physics of the Earth and Planetary Interiors*, 25(4), 297 – 356. doi: 10.1016/
 451 0031-9201(81)90046-7
- 452 Dziewonski, A. M., Bloch, S., & Landisman, M. (1969). A technique for the analy-
 453 sis of transient seismic signals. *Bull. Seism. Soc. Am.*, 59, 427 – 444. doi: 10
 454 .1785/BSSA0590010427
- 455 Grotzinger, J. P., Gupta, S., Malin, M. C., Rubin, D. M., Schieber, J., Siebach, K.,
 456 ... Wilson, S. A. (2015). Deposition, exhumation, and paleoclimate of an
 457 ancient lake deposit, Gale crater, Mars. *Science*, 350(6257), aac7575. doi:
 458 10.1126/science.aac7575
- 459 Grotzinger, J. P., & Milliken, R. E. (2012). The Sedimentary Rock Record of Mars:
 460 Distribution, Origins, and Global Stratigraphy..
- 461 Harkrider, D., & Anderson, D. L. (1962). Computation of surface wave disper-
 462 sion for multilayered anisotropic media. *Bulletin of the Seismological Society of
 463 America*, 52(2), 321–332. doi: 10.2307/1779766
- 464 Head, J. W., Ivanov, M. A., Hiesinger, H., Kreslavsky, M. A., Pratt, S., & Thomson,

- 465 B. J. (2001). Oceans in the northern lowlands of Mars?: Further tests using
466 MGS data. In *Lunar Planet. Sci. XXXII*.
- 467 Herrmann, R. B. (2013). Computer programs in seismology: An evolving tool for in-
468 struction and research. *Seismological Research Letters*, *84*(6), 1081–1088.
- 469 Horleston, A. C., Clinton, J. F., Ceylan, S., Giardini, D., Charalambous, C., Irv-
470 ing, J. C. E., ... Banerdt, W. B. (2022). The far side of Mars: Two distant
471 marsquakes detected by InSight. *The Seismic Record*, *2*(2), 88–99. doi:
472 10.1785/0320220007
- 473 InSight Mars SEIS Data Service. (2019a). *nsight seis data bundle. pds geosciences*
474 *(geo) node*. Retrieved from <https://doi.org/10.17189/1517570> doi: 10
475 .17189/1517570
- 476 InSight Mars SEIS Data Service. (2019b). *Seis raw data, insight mission. ipgp,*
477 *jpl, cnes, ethz, icl, mps, isae-superaero, lpg, mfsc*. IPGP, JPL, CNES, ETHZ,
478 ICL, MPS, ISAE-Supaero, LPG, MFSC. Retrieved from [https://doi.org/](https://doi.org/10.18715/SEIS.INSIGHT.XB.2016)
479 [10.18715/SEIS.INSIGHT.XB.2016](https://doi.org/10.18715/SEIS.INSIGHT.XB.2016) doi: 10.18715/SEIS.INSIGHT.XB.2016
- 480 InSight Marsquake Service. (2020). *Mars Seismic Catalogue, InSight Mission;*
481 *V1 2/1/2020. ETHZ, IPGP, JPL, ICL, ISAE-Supaero, MPS, Univ Bristol.*
482 *Dataset*. doi: <https://doi.org/10.12686/a6>
- 483 InSight Marsquake Service. (2022a). *Mars seismic catalogue, insight mission; v11*
484 *2022-07-01*. ETHZ, IPGP, JPL, ICL, Univ. Bristol. Retrieved from [https://](https://www.insight.ethz.ch/seismicity/catalog/v11)
485 www.insight.ethz.ch/seismicity/catalog/v11 doi: 10.12686/a17
- 486 InSight Marsquake Service. (2022b). *Mars seismic catalogue, insight mission; v12*
487 *2022-10-01*. ETHZ, IPGP, JPL, ICL, Univ. Bristol. Retrieved from [https://](https://www.insight.ethz.ch/seismicity/catalog/v12)
488 www.insight.ethz.ch/seismicity/catalog/v12 doi: 10.12686/a18
- 489 Jiang, C., Schmandt, B., Farrell, J., Lin, F.-C., & Ward, K. M. (2018). Seismically
490 anisotropic magma reservoirs underlying silicic calderas. *Geology*, *46*(8), 727-
491 730. doi: 10.1130/G45104.1
- 492 Karato, S.-i., & Wu, P. (1993). Rheology of the Upper Mantle - a Synthesis. *Sci-*
493 *ence*, *260*(5109), 771 – 778. doi: 10.1126/science.260.5109.771
- 494 Kawamura, T., Clinton, J. F., Zenhäusern, G., Ceylan, S., Horleston, A. C., Dah-
495 men, N. L., ... Banerdt, W. B. (2022). Largest marsquake ever detected by
496 InSight: S1222a.
497 (submitted)

- 498 Khan, A., Ceylan, S., van Driel, M., Giardini, D., Lognonné, P., Samuel, H., . . . oth-
499 ers (2021). Upper mantle structure of mars from insight seismic data. *Science*,
500 *373*(6553), 434–438.
- 501 Kim, D., Banerdt, W. B., Ceylan, S., Giardini, D., Lekić, V., Lognonné, P., . . . Pan-
502 ning, M. P. (2022). Surface waves and crustal structure on Mars. *Science*,
503 *378*(6618), 417–421. doi: 10.1126/science.abq7157
- 504 Kim, D., Davis, P., Lekić, V., Maguire, R., Compaire, N., Schimmel, M., . . .
505 Banerdt, W. B. (2021). Potential Pitfalls in the Analysis and Structural Inter-
506 pretation of Seismic Data from the Mars InSight Mission. *Bulletin of the Seis-*
507 *mological Society of America*, *111*(6), 2982–3002. doi: 10.1785/0120210123
- 508 Kim, D., Lekić, V., Irving, J. C. E., Schmerr, N., Knapmeyer-Endrun, B., Joshi, R.,
509 . . . Banerdt, W. B. (2021). Improving Constraints on Planetary Interiors With
510 PPs Receiver Functions. *Journal of Geophysical Research. Planets*, *126*(11),
511 e2021JE006983. doi: 10.1029/2021je006983
- 512 Knapmeyer-Endrun, B., Panning, M. P., Bissig, F., Joshi, R., Khan, A., Kim, D., . . .
513 Banerdt, W. B. (2021). Thickness and structure of the martian crust from In-
514 Sight seismic data. *Science*, *373*(6553), 438–443. doi: 10.1126/science.abf8966
- 515 Koper, K. D., Wyssession, M. E., & Wiens, D. A. (1999). Multimodal function op-
516 timization with a niching genetic algorithm: A seismological example. *Bulletin*
517 *of the Seismological Society of America*, *89*(4), 978–988.
- 518 Latypov, R., Chistyakova, S., Grieve, R., & Huhma, H. (2019). Evidence for ig-
519 neous differentiation in Sudbury Igneous Complex and impact-driven evo-
520 lution of terrestrial planet proto-crusts. *Nature Communication*, *10*. doi:
521 10.1038/s41467-019-08467-9
- 522 Li, J., Beghein, C., Lognonné, P., McLennan, S. C., Wieczorek, M., Panning, M. P.,
523 . . . Banerdt, W. B. (2022). Analysis of minor- and major-arc rayleigh waves
524 on mars across the crustal dichotomy boundary. *Geophysical Research Letters*.
525 (submitted)
- 526 Li, J., Beghein, C., Wookey, J., Davis, P., Lognonné, P., Schimmel, M., . . .
527 Banerdt, W. B. (2022). Evidence for crustal seismic anisotropy at the In-
528 Sight lander site. *Earth and Planetary Science Letters*, *593*, 117654. doi:
529 10.1016/j.epsl.2022.117654

- 530 Li, J., Chen, M., Koper, K. D., Zhou, T., Xi, Z., Li, S., & Li, G. (2021). Fasttrip: A
 531 fast mpi-accelerated 1d triplication waveform inversion package for constrain-
 532 ing mantle transition zone discontinuities. *Seismological Research Letters*,
 533 *92*(4), 2647–2656.
- 534 Lognonné, P., Banerdt, W. B., Giardini, D., Pike, W. T., Christensen, U., Laudet,
 535 P., . . . Wookey, J. (2020). SEIS: Insight’s Seismic Experiment for In-
 536 ternal Structure of Mars. *Space Science Reviews*, *215*(1), 1 – 170. doi:
 537 10.1007/s11214-018-0574-6
- 538 Marinova, M., Aharonson, O., & Asphaug, E. (2008). Mega-impact formation of the
 539 Mars hemispheric dichotomy. *Nature*, *453*(7199). doi: 10.1038/nature07070
- 540 McLennan, S. M. (2012). *Geochemistry of sedimentary processes on mars* (Vol. 102;
 541 J. P. Grotzinger & R. E. Milliken, Eds.). doi: 10.1007/978-3-0348-8777-9_2
- 542 Montagner, J.-P. (1994). Can Seismology Tell Us Anything About Convection in the
 543 Mantle. *Reviews of Geophysics*, *32*(2), 115 – 137. doi: 10.1029/94rg00099
- 544 Montagner, J.-P. (1998). Where can seismic anisotropy be detected in the Earth’s
 545 mantle? In boundary layers. *Pure and Applied Geophysics*, *151*(Chapter 2),
 546 223 – 256. doi: 10.1007/978-3-0348-8777-9_2
- 547 Moschetti, M., Ritzwoller, M., Lin, F., & Yang, Y. (2010). Seismic evidence for
 548 widespread western-us deep-crustal deformation caused by extension. *Nature*,
 549 *464*(7290), 885–889.
- 550 Nimmo, F., & Tanaka, K. (2005). Early crustal evolution of mars. *Annual Review of*
 551 *Earth and Planetary Sciences*, *33*(1), 133–161.
- 552 Nishimura, C. E., & Forsyth, D. W. (1989). The Anisotropic Structure of the Up-
 553 per Mantle in the Pacific. *Geophysical Journal*, *96*(2), 203 – 229. doi: 10.1111/
 554 j.1365-246x.1989.tb04446.x
- 555 Panning, M. P., Banerdt, W. B., Beghein, C., Carrasco, S., Ceylan, S., Clinton,
 556 J. F., . . . Stähler, S. C. (2022). Locating the largest event observed on Mars
 557 with multi-orbit surface waves. *Geophysical Research Letters*. (submitted)
- 558 Planke, S. (1994). Geophysical response of flood basalts from analysis of wire line
 559 logs: Ocean Drilling Program Site 642, Vøring volcanic margin. *Journal of*
 560 *Geophysical Research: Solid Earth*, *99*(B5). doi: 10.1029/94jb00496
- 561 Rodriguez, J., Baker, V., Liu, T., Zarroca, M., Travis, B., Hui, T., . . . Kargel,
 562 J. S. (2019). The 1997 Mars Pathfinder Spacecraft Landing Site: Spillover

- 563 Deposits from an Early Mars Inland Sea. *Scientific Reports*, 9(4045). doi:
564 10.1038/s41598-019-39632-1
- 565 Sayers, C. (1998). Long-wave seismic anisotropy of heterogeneous reservoirs. *Geo-*
566 *physical Journal International*, 132(3), 667-673. doi: 10.1046/j.1365-246X.1998
567 .00456.x
- 568 Scholz, J.-R., Widmer-Schnidrig, R., Davis, P., Lognonné, P., Pinot, B., Garcia,
569 R. F., ... Banerdt, W. B. (2020). Detection, Analysis, and Removal of
570 Glitches From InSight's Seismic Data From Mars. *Earth and Space Sci-*
571 *ence*, 7(11), e2020EA001317. (e2020EA001317 10.1029/2020EA001317) doi:
572 10.1029/2020EA001317
- 573 Shapiro, M., Nikolai, Ritzwoller, M. H., Molnar, P., & Levin, V. (2004). Thin-
574 ning and flow of tibetan crust constrained by seismic anisotropy. *Science*,
575 305(5681), 233-236. doi: 10.1126/science.1098276
- 576 Stähler, S. C., Khan, A., Banerdt, W. B., Lognonné, P., Giardini, D., Ceylan, S.,
577 ... others (2021). Seismic detection of the martian core. *Science*, 373(6553),
578 443-448.
- 579 Villanueva, G. L., Mumma, M. J., Novak, R. E., Köpff, H. U., Hartogh, P., En-
580 crenaz, T., ... Smith, M. D. (2015). Strong water isotopic anomalies in
581 the martian atmosphere: Probing current and ancient reservoirs. *Science*,
582 348(6231), 218-221. doi: 10.1126/science.aaa3630
- 583 Weidner, E., Beghein, C., Huang, Q., & Schmerr, N. (2022). Upper mantle radial
584 anisotropy under the Indian Ocean from higher mode surface waves and a
585 hierarchical transdimensional approach. *Geophysical Journal International*,
586 228(1), 78-101. doi: 10.1093/gji/ggab340
- 587 Weiss, T., Siegesmund, S., Rabbal, W., Bohlen, T., & Pohl, M. (1999). Seismic Ve-
588 locities and Anisotropy of the Lower Continental Crust: A Review. *Pure and*
589 *Applied Geophysics*, 156(1), 97-122. doi: 10.1007/s000240050291
- 590 Wieczorek, M. A., Broquet, A., McLennan, S. M., Rivoldini, A., Golombek, M., An-
591 tonangeli, D., ... Banerdt, W. B. (2022). InSight constraints on the global
592 character of the Martian crust. *Journal of Geophysical Research: Planets*. doi:
593 10.1029/2022je007298
- 594 Wilhelms, D., & Squyres, S. (1984). The martian hemispheric dichotomy may be
595 due to a giant impact. *Nature*, 309, 138 - 140. doi: 10.1038/309138a0

596 Yuan, H., & Romanowicz, B. (2010). Lithospheric layering in the North American
597 craton. *Nature*, *466*(7310), 1063 – 1068. doi: 10.1038/nature09332